

Article

Development of Vitroceramic Coatings and Analysis of Their Suitability for Biomedical Applications

Sorin-Ion Jinga ¹, Michael Skokin ¹, Bogdan-Stefan Vasile ¹, Izabela Constantinoiu ^{1,2}, Dana Miu ², Mihaela Bacalum ³ and Cristina Busuioc ^{1,*}

¹ Department of Science and Engineering of Oxide Materials and Nanomaterials, University POLITEHNICA of Bucharest, RO-011061 Bucharest, Romania; sorinionjinga@yahoo.com (S.-I.J.); mike.skokin@gmail.com (M.S.); bogdan.vasile@upb.ro (B.-S.V.); constantinoiu.izabela@yahoo.com (I.C.)

² National Institute for Laser, Plasma and Radiation Physics, RO-077125 Magurele, Romania; dana_miu2001@yahoo.com

³ Horia Hulubei National Institute of Physics and Nuclear Engineering, RO-077125 Magurele, Romania; bmihaela@nipne.ro

* Correspondence: cristina.busuioc@upb.ro

Received: 18 September 2019; Accepted: 14 October 2019; Published: 16 October 2019



Abstract: Within the field of tissue engineering, thin films have been studied to improve implant fixation of metallic or ceramic materials in bone, connective tissue, oral mucosa or skin. In this context, to enhance their suitability as implantable devices, titanium-based substrates received a superficial vitroceramic coating by means of laser ablation. Further, this study describes the details of fabrication and corresponding tests in order to demonstrate the bioactivity and biocompatibility of the newly engineered surfaces. Thus, the metallic supports were covered with a complex material composed of SiO₂, P₂O₅, CaO, MgO, ZnO and CaF₂, in the form of thin layers via a physical deposition techniques, namely pulsed laser deposition. The resulting products were characterized by X-ray diffraction, Fourier-transform infrared spectroscopy, scanning and transmission electron microscopy coupled with energy dispersive X-ray spectroscopy, selected area electron diffraction, and electron energy loss spectroscopy. It was found that a higher substrate temperature and a lower working pressure lead to the highest quality film. Finally, the samples biocompatibility was assessed and they were found to be bioactive after simulated body fluid soaking and biocompatible through the MTT cell viability test.

Keywords: vitroceramic; coatings; pulsed laser deposition; bioactivity; metallic implants

1. Introduction

Developing biocompatible implantable artifacts is a goal that, even today, is still being pursued, given that the targeted biological systems are very complex and need long trials for design, fabrication, testing and implementation. If the mechanical attributes of an implantable artifact are relatively well understood [1–3], it is not so when it comes to the its interaction with the immune system of the recipient [4–6].

The earliest implants were handcrafted out of animal bone and, later on, diverse materials, like natural polymers (gutta-percha [7], rubber [8], cellulose [9], collagen [10]), were employed with varying degrees of success. Depending on specific applications and according to the mechanical requirements, there are competing materials, such as ceramics [11–13] and composites [14]. However, for implants that experience large flexural loads, a metal is always required. The best results were obtained by using titanium and its alloys [15,16], most remarkably Ti–6Al–4V (no longer in use due to Al and V ion leakage), Ti–13Nb–13Zr and Ti–12Mo–6Zr [17]. Notably, an alloy of Ti–3Au shows excellent mechanical and biochemical properties, but unfortunately it is prohibitively expensive [18]. Several

drawbacks, like fibrous tissue growth, slow osseointegration and reduced close contact with the host bone, were noticed upon wider use of titanium alloy implants [19]. Thus, the quest is to develop a composite material with all the mechanical properties of titanium alloys, encapsulated in a leak-proof ceramic, that can be biologically preactivated prior to implant [20,21].

With the advent of laser-based additive manufacturing [22], such composite material is now a reality. In this case, a commercial or custom-made ceramic target is ablated by a pulsed laser, a plume of plasma is generated and directed towards the metallic substrate, upon which it settles, forming a thin layer that physically binds to the support [23,24]. Our research group has already reported the growth of nanostructured akermanite-based thin films by pulsed laser deposition, with good biocompatibility and bioactivity [25]. Since both the target characteristics and processing conditions strongly influence the properties of the final coatings [26], more studies are necessary in order to elucidate which are the driven factors and optimized set of parameters.

Thus, the aim of this work is to produce a material that is durable and readily implantable. A type of vitroceramic coatings on titanium substrates were developed, characterized and then immersed in simulated biological fluid to be coated with a hydroxyapatite-like layer and demonstrate its bioactivity [27,28]. Further biological tests indicated that, indeed, this combination of materials resulted in an artifact that responds well to the in vitro cell proliferation.

2. Materials and Methods

2.1. Thin Films Deposition

The mineral coatings were obtained by pulsed laser deposition, using a target that was synthesized in our laboratory using a wet-chemistry approach; the details of this processing step, as well as the characteristics of the final ceramic disc, were included in a previous paper [25]. Briefly, the target composition was $0.38\text{SiO}_2\text{--}0.04\text{P}_2\text{O}_5\text{--}0.3525\text{CaO--}0.18\text{MgO--}0.04\text{ZnO--}0.0075\text{CaF}_2$, alkoxides and nitrates being mainly employed as precursors for the sol-gel procedure. The gel formed was dried, calcined, shaped and presintered, then the resulting powder was granulated, shaped and sintered in optimized conditions. The reasons for choosing such oxide system are detailed in previous papers [11,25]. Mainly, the content of SiO_2 , CaO and MgO ensures the positioning of the composition within the primary crystallization field of akermanite in the corresponding ternary system; SiO_2 and P_2O_5 are network formers, while CaO , MgO and ZnO are network modifiers for glass; P_2O_5 also contributes to apatite formation; CaO and MgO likewise sustain the mineralization process when introduced into the physiological environment; ZnO favours the emergence of a high surface area, while CaF_2 modifies the biochemical processes in a beneficial way.

The final target was used for the deposition experiments on titanium substrates, namely pure and thin titanium plates cut into pieces of $1 \times 1 \text{ cm}^2$. The values of the constant and variable parameters are listed in Tables 1 and 2. Basically, the influence of the substrate temperature and oxygen pressure in the working chamber on the physicochemical properties and biological response was studied.

Table 1. Values of the constant parameters for the deposition of the coatings.

Parameter	Value
Laser wavelength	532 nm
Repetition rate	10 Hz
Number of pulses	26,000 pulses
Energy per pulse	81 mJ

Table 2. Values of the variable parameters for the deposition of the coatings.

Sample Name	Substrate Temperature (°C)	Oxygen Pressure (mTorr)
Film A	250	100
Film B	350	
Film C	250	200
Film D	350	

2.2. Physicochemical Characterization

The characterization methods included: grazing incidence X-ray diffraction (XRD) with a PANalytical Empyrean diffractometer (Malvern Panalytical, Royston, UK), with 0.5° incidence angle, 2 θ ranging between 10° and 80°; Fourier-transform infrared spectroscopy (FTIR) with a Thermo Scientific Nicolet 6700 spectrophotometer (Thermo Fisher Scientific, Waltham, MA, USA), the wavenumber ranging between 400 and 1300 cm⁻¹; scanning electron microscopy (SEM), coupled with energy-dispersive X-ray spectroscopy (EDX) with a FEI Quanta Inspect F electron microscope (FEI, Hillsboro, OR, USA); transmission electron microscopy both in conventional (TEM) and scanning (STEM) mode, coupled with selected area diffraction (SAED) and electron energy loss spectroscopy (EELS), with a Titan Themis transmission electron microscope (FEI, Hillsboro, OR, USA).

2.3. Biological Characterization

The biological evaluation was performed through in vitro tests; simulated body fluid (SBF) soaking for 14 days, at 37 °C, the testing solution being prepared according to Kokubo et al. [29], as well as MTT assay (cell viability) [30] on human fibroblast BJ cells, the values being read at 24 h.

In detail, human fibroblast BJ cells (ATCC CRL-2522, Manassas, VA, USA) were grown in minimal essential medium (MEM) supplemented with 2 mM L-Glutamine, 10% fetal calf serum (FCS), 100 units/mL of penicillin and 100 µg/mL of streptomycin, at 37 °C, in a humidified incubator, under an atmosphere containing 5% CO₂. All cell cultivation media and reagents were purchased from Biochrom AG (Berlin, Germany).

Cell viability was evaluated using MTT (3-(4,5-dimethylthiazol-2-yl)-2,5-diphenyltetrazolium bromide) assay. First, the samples to be investigated were sterilized and placed in a 12 well plate. The cells (50,000 cells/well) were seeded over the specimens and cultured for 24 h in medium. Cells seeded in an empty well were employed as negative Control. After 24 h incubation, the medium was changed and MTT solution was added to each well to a final concentration of 1 mg/mL and incubated with the cells for additional 4 h, at 37 °C. Finally, the medium was collected and dimethyl sulfoxide (DMSO) was used to dissolve the insoluble formazan product formed by the mitochondria of living cells. The absorbance of the samples was recorded at 570 nm using a plate reader (Mithras 940, Berthold). The data were corrected for the background and the percentage of viable cells was obtained using the equation below.

$$\text{Cell viability} = [(A_{570} \text{ of treated cells}) / (A_{570} \text{ of untreated cells})] \times 100 [\%] \quad (1)$$

After incubation for 24 h with the specimens, the morphological changes induced in the cells were observed under a bright-field microscope CKX53 (Olympus, Tokyo, Japan) using a 20× objective and photographed with a WAT-902H camera (Watec, Saint-Lambert-la-Potherie, France).

3. Results and Discussion

3.1. Physicochemical Characterization

The ceramic target employed for the PLD experiments was fabricated in our laboratory, being thermally treated at 1200 °C; the phase composition consisted of akermanite as major crystalline phase and diopside as minor crystalline phase, with a relatively dense appearance [25].

Figure 1a shows the XRD patterns of the four thin films grown by laser ablation on titanium substrates in different experimental conditions (Table 2). As can be seen, the most intense signals are attributed to the metallic supports made of hexagonal titanium (ICDD 00-044-1294) due to the low thickness of the deposited layers. Even though the investigation was carried out at grazing incidence, for most of the samples, only small diffraction peaks assigned to tetragonal akermanite— $\text{Ca}_2\text{MgSi}_2\text{O}_7$ (ICDD 00-035-0592) were identified. However, in the case of Film D, an increase in signal emerged, which can be associated with the highest values of the variable processing parameters, substrate temperature— 350°C and oxygen pressure— 200 mTorr . Another fact that has to be taken into account is related to the shape of the XRD patterns at low angles, with the occurrence of an amorphous halo due to the existence of a short range order in glassy masses; basically, the structural units maintain their periodicity only at the level of the nearest neighbours, while the overall structure is macroscopically isotropic. In this light, it can be stated that the coatings produced are vitroc ceramic in nature, meaning a vitreous matrix and crystals of akermanite distributed within it.

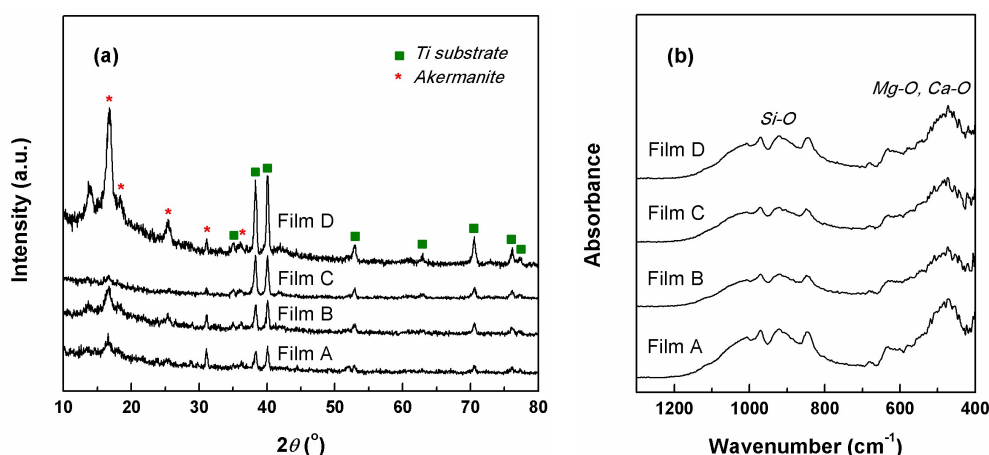


Figure 1. (a) X-ray diffraction (XRD) patterns and (b) Fourier-transform infrared spectroscopy (FTIR) spectra of the coatings grown by pulsed laser deposition.

The films structure is also demonstrated through the FT-IR spectra, displayed in Figure 1b. Specific vibrational bands appear for all coatings, these being easily correlated with the vibrations of cation-oxygen bonds, especially in the case of those cations having the highest three concentrations within the deposited materials. Thus, a group of bands were assigned to Si–O bonds movements, while below 600 cm^{-1} , the vibrations of alkaline earth—oxygen bonds (Ca–O and Mg–O) were identified [31].

The SEM images achieved on the surface of the films (Figure 2) highlight the formation of continuous and compact layers on top of titanium substrates, with spherical agglomerations of particles from place to place. The average grain size seemed to be slightly different from one sample to another, but ranging in $10\text{--}50\text{ nm}$ interval, with a visible decrease when raising the substrate temperature, an aspect that has been reported before [25]. Moreover, at lower magnification, specific deposition droplets could be observed, mostly for the lower temperature substrate and oxygen pressure, as well as the substrate surface features, with a certain rough pattern developed during metallic plates cutting and polishing. In this way, a reduced thickness was confirmed, a fact that will be clarified only by cross-sectional investigations. All morphological variations are explicable on the basis of the energy provided to the substrate from behind and pressure applied on the coating from the front.

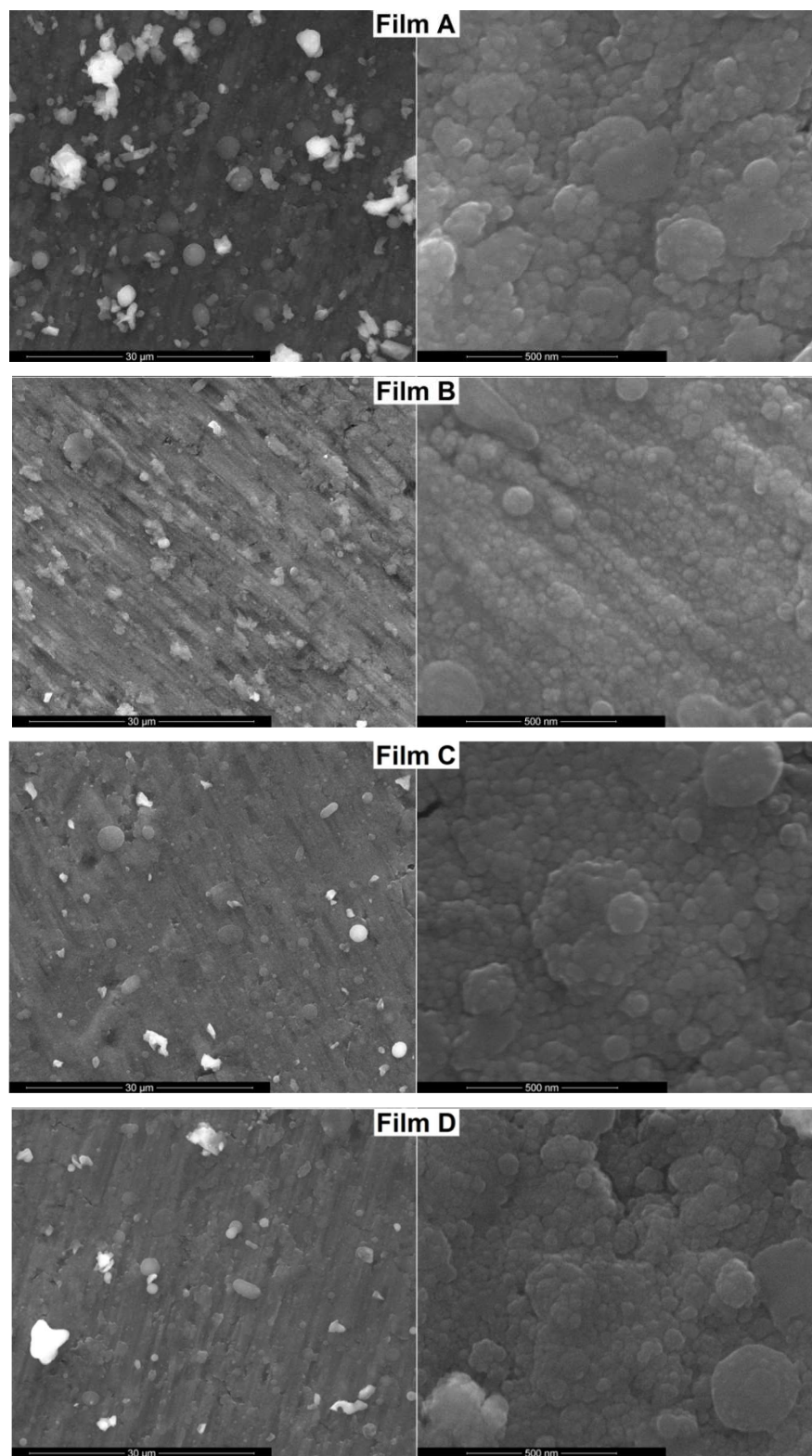


Figure 2. Scanning electron microscopy (SEM) images of the coatings grown by pulsed laser deposition.

The composition transfer from the target to the films was also validated through the EDX spectra presented in Figure 3. Besides the intense maxima of Ti, signals of all important elements were detected (Si, P, Ca, Mg, Zn, and O), the ratios between them being similar to the ratio in the designed material.

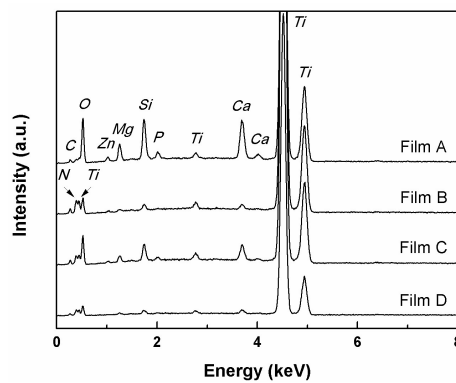


Figure 3. Energy-dispersive X-ray spectroscopy (EDX) spectra of the coatings grown by pulsed laser deposition.

In order to evaluate the thickness of the films and the dimension of the crystalline domains, the depositions were also performed on silicon wafers, since their processing for TEM investigation is possible, as opposed to titanium plates. Film A was selected for such analysis because it gave the best biological response when it comes to the bioactive potential. This behavior is not surprising if we take into account that this sample was fabricated at the lower substrate temperature and oxygen pressure, leading to a structure and morphology more prone to interactions with the simulated body fluid. The vitroceraic layer thickness was determined to be around 160 nm (Figure 4a,b), with small variations due to the droplets presence. Figure 4c reveals the interface between the silicon substrate and grown coating, while Figure 4d shows the interface between the deposited film and the resin used to bond the two identical TEM samples face to face. In both cases, the interface is clean and straight, with a very good adhesion to silicon plate and a low roughness on the other side. The HRTEM image from Figure 4e evidences the encapsulated crystals, which have sizes below 5 nm and for which the SAED pattern (Figure 4f) indicated the crystalline planes typical of akermanite.

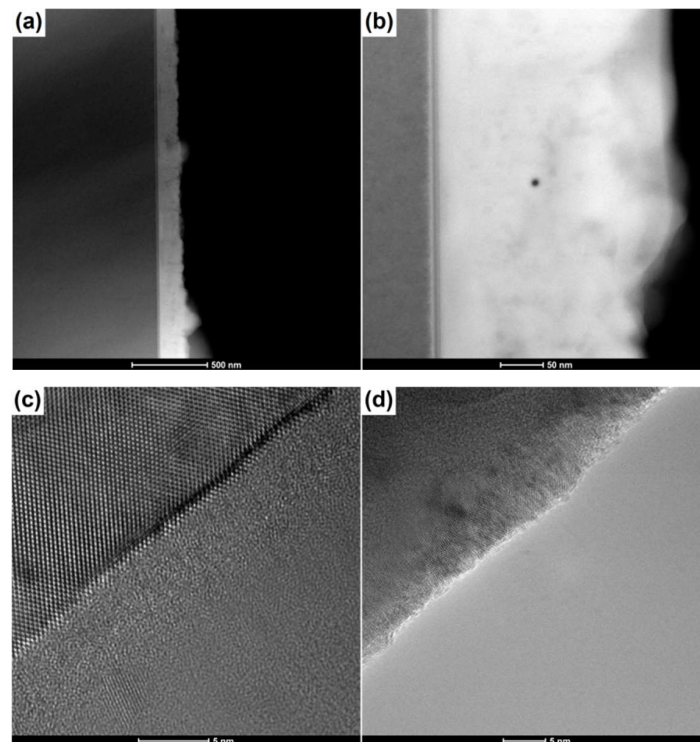


Figure 4. *Cont.*

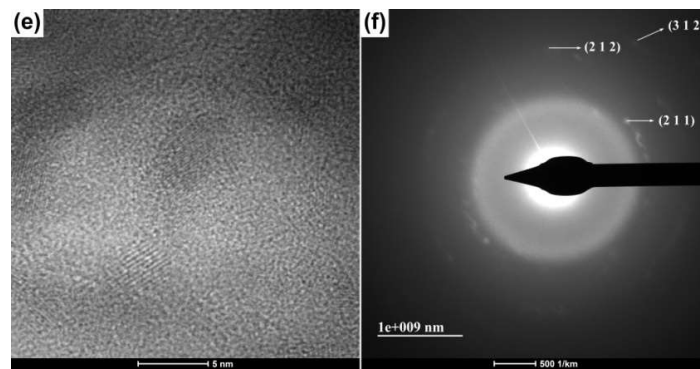


Figure 4. (a,b) Transmission electron microscopy (TEM) image, (c–e) HRTEM images and (f) selected area diffraction (SAED) pattern of Film A.

Going to the elemental distribution, Figure 5 displays the corresponding EELS maps, together with the associated STEM image. Thus, all important elements (Si, P, Ca, Mg, Zn, O) had a homogenous distribution even at nanometric scale, a fact that indicates a glass composition that resembles with akermanite. Comparing these results with the previously reported data on ceramic thin films obtained from the same target [25], it can be concluded that the modification of laser wavelength from 355 to 532 nm has a pronounced impact on the structural features of the deposited layers. In other words, an increase in radiation wavelength is translated into a lower quantity of energy provided to the target material, which is individualized through the appearance of partially crystalline coatings instead of almost completely crystalline ones. This characteristic will further influence the biological behavior in different experimental conditions, since the vitreous matrix will provide another background through the less strong chemical bonds.

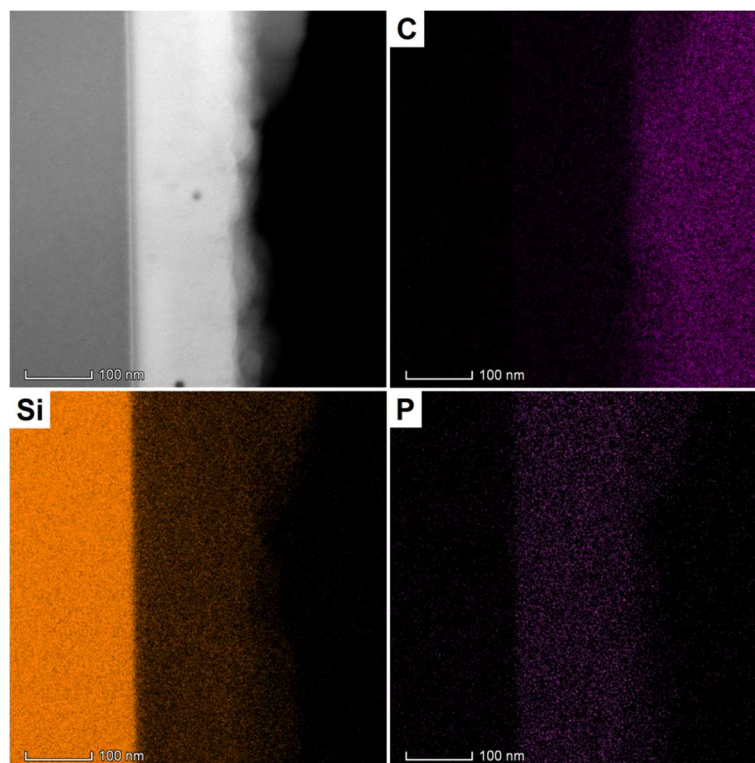


Figure 5. *Cont.*

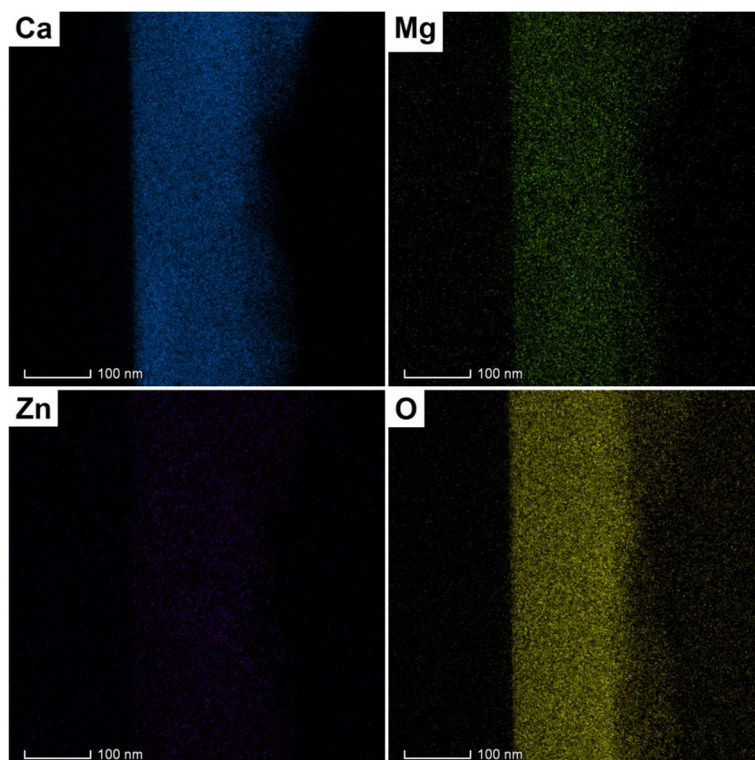


Figure 5. Electron energy loss spectroscopy (EELS) mapping of Film A.

3.2. Biological Characterization

The bioactivity of the nanostructured thin films was examined in SBF solution, by soaking the samples for 14 days, in standard conditions. The deposited layers are expected to influence the *in vitro* response and that is way the potential changes were evaluated through SEM investigation (Figure 6). The surface morphology is quite different from one sample to another, which can be linked to distinct kinetics for apatite formation. Even though all coatings are overlaid with apatitic phases, only in the case of Film A and Film C, those obtained at 250 °C substrate temperature, the quantity is significant and covers most of the vitroceraic surface; the second one individualizes through an interconnected porosity and areas of uneven growth. Moreover, the newly formed layer is composed of fine globular structures with diameters below 50 nm, bound in a laced network and made up of particles of few nanometers. As respects to the other two coatings, Film B and D, their capability of inducing apatite generation in SBF solution within 14 days of incubation is only partial, the corresponding SEM images exhibiting a thin and discontinuous layer of fine and loose structures, smaller than 10 nm, that seem to be in the process of developing; Film D stands out through the islands of flat deposits that sometimes join into a more extended network. It can be concluded that a better bioactivity is linked to a lower substrate temperature, parameter that provide films more labile in the interaction with the surrounding fluids due to the weaker bonds between atoms.

The samples impact on BJ cells viability and morphology are presented in Figure 7. The proliferation of the cells for the tested conditions was checked and plotted in Figure 7a. Using MTT assay, the percentage of viable cells in comparison with Control cells was evaluated. The most toxic effect was produced by Film A, which decreased the viability of the cells with approximately 20%. When BJ cells grew in the presence of Film B and Film C, the corresponding values were 87% and 84%, respectively. The smallest influence was observed in the case of Film D, which only decreased the viability of the cells as compared to Control cells with 9%. However, considering the error bars, all samples are integrated in the same trend, with a low degree of cytotoxic effect.

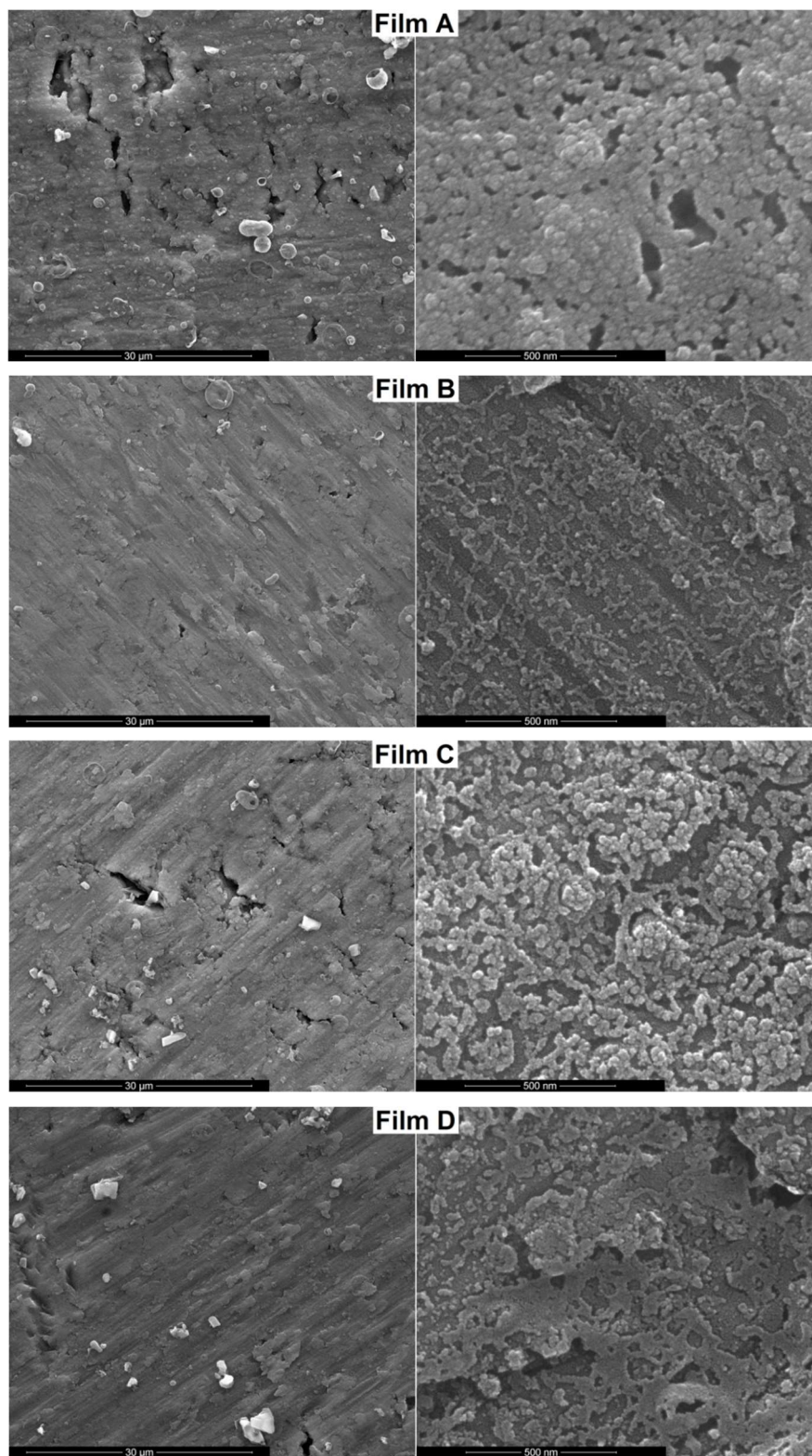


Figure 6. SEM images of the coatings after immersion in simulated body fluid (SBF) for 14 days.

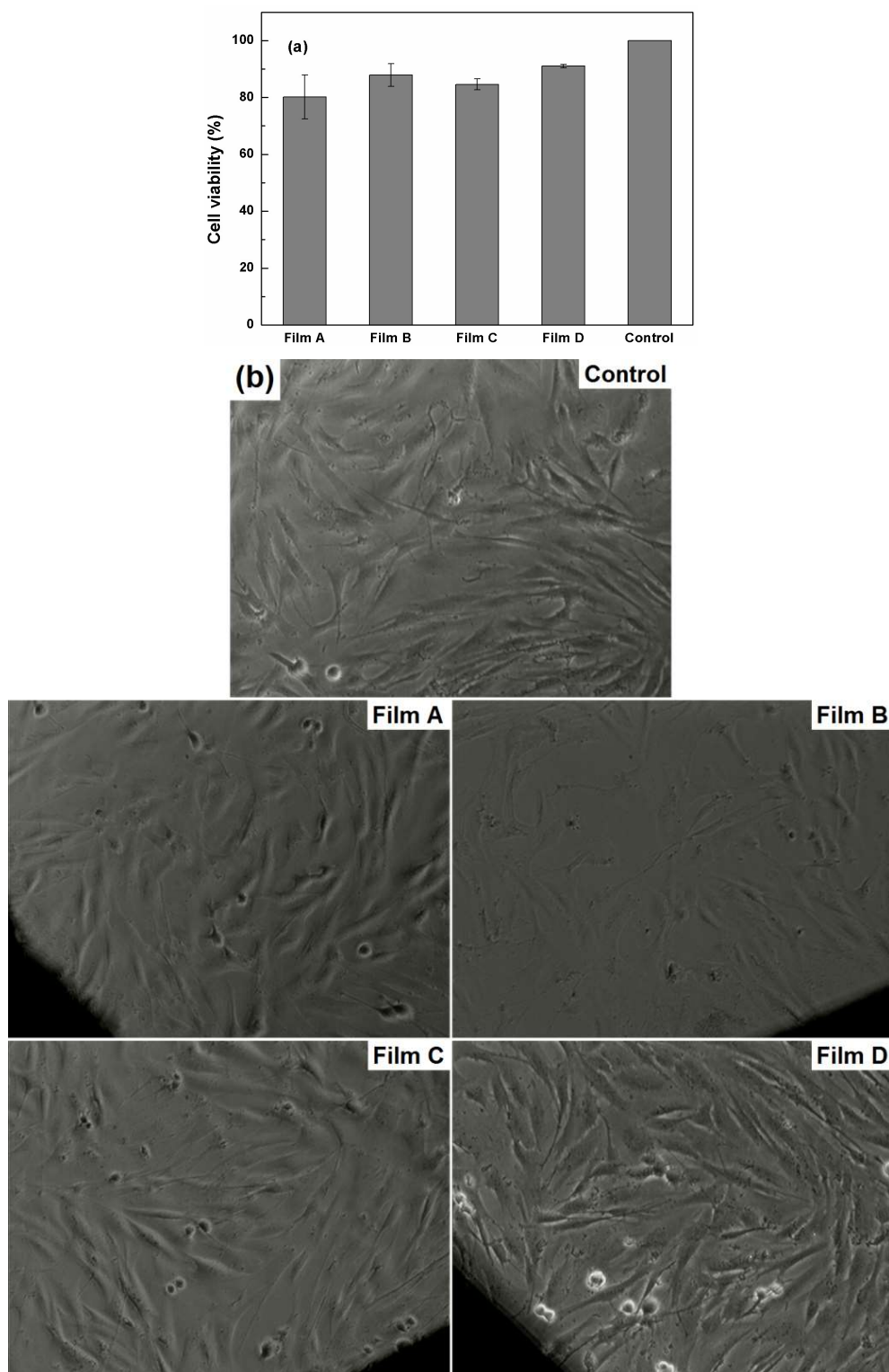


Figure 7. (a) Cell viability by MTT assay and (b) optical microscopy images (20× magnification) of BJ cells grown for 24 h in the presence/absence of the samples.

Further, in the image of Control cells (Figure 7b), the specific morphology of fibroblast cells, fusiform and elongated, can be observed. When the cells were cultured in the presence of the four coated metallic substrates, the morphology of the cells was not affected; there were no cells or debris floating in the medium and only a small number of cells started to round up.

In conclusion, akermanite received a significant attention in the last few years due to its excellent in vitro bioactivity, biocompatibility and biodegradability combined with good mechanical properties [25,32–34]. However, most of these papers have been dedicated to powders or scaffolds and less to thin films, which imposes the need for more complex studies in this field, in order to understand the implications of coating bioinert metallic or ceramic implants with such compositions.

4. Conclusions

By starting from a laboratory-made ceramic target belonging to $\text{SiO}_2\text{--P}_2\text{O}_5\text{--CaO--MgO--ZnO--CaF}_2$ system and based on akermanite as the main crystalline phase, thin films were grown on titanium substrates by pulsed laser deposition. Two parameters were varied, substrate temperature and oxygen pressure, in order to achieve coatings with different structural and morphological features. All resulting layers had a vitroceramic character, with crystals of akermanite distributed within the parent glassy matrix. From a morphological point of view, the coatings are nanostructured, continuous and have a thickness between 100 and 200 nm.

The bioactivity of the samples was proven to be dependent on the processing conditions. The substrate temperature is the underlying factor that dictates the quality of the initial vitroceramic film and subsequently that of the deposited apatite layer; oxygen pressure appears to be of secondary importance. Mainly, a lower substrate temperature is translated into a higher bioactive potential. As far as biocompatibility is concerned, the developed thin films can be considered biocompatible as they showed no or small toxicity towards BJ cells after a 24 h treatment. The seeded cells spread uniformly on the surfaces and maintained their elongated shape, indicating the cytocompatibility of the tested specimens. Based on these results, such materials can be further used in safely designing new materials with biomedical applications.

Future research might be directed towards the deposition of such coatings on ceramic surfaces via laser ablation to create engineered surfaces with tunable roughness so that to control the cellular adhesion. Another direction might aim the biofunctionalization of the grown films with highly active peptides in order to improve osteoblasts attachment and implant osseointegration.

Author Contributions: Conceptualization, S.-I.J. and C.B.; methodology, C.B. and D.M.; validation, S.-I.J.; investigation, M.S., B.-S.V., I.C., D.M., M.B. and C.B.; resources, D.M., M.B. and C.B.; writing-original draft preparation, C.B.; writing-review and editing, C.B.; supervision, S.-I.J.

Funding: This research received no external funding.

Conflicts of Interest: The authors declare no conflict of interest.

References

1. Estevez, E.P.; Burganova, R.M.; Lysogorskii, Y.V. Computer simulation of the elastic properties of titanium alloys for medical applications. *J. Eng. Phys. Thermophys.* **2016**, *89*, 1344–1348. [[CrossRef](#)]
2. Soro, N.; Attar, H.; Brodie, E.; Veidt, M.; Molotnikov, A.; Dargusch, M.S. Evaluation of the mechanical compatibility of additively manufactured porous Ti–25Ta alloy for load-bearing implant applications. *J. Mech. Behav. Biomed. Mater.* **2019**, *97*, 149–158. [[CrossRef](#)] [[PubMed](#)]
3. Wang, J.; Zhang, S.; Sun, Z.; Wang, H.; Ren, L.; Yang, K. Optimization of mechanical property, antibacterial property and corrosion resistance of Ti–Cu alloy for dental implant. *J. Mater. Sci. Technol.* **2019**, *35*, 2336–2344. [[CrossRef](#)]
4. Shah, F.A.; Thomsen, P.; Palmquist, A. Osseointegration and current interpretations of the bone-implant interface. *Acta Biomater.* **2019**, *84*, 1–15. [[CrossRef](#)]
5. Hu, C.; Ashok, D.; Nisbet, D.R.; Gautam, V. Bioinspired surface modification of orthopedic implants for bone tissue engineering. *Biomaterials* **2019**, *219*, 119366. [[CrossRef](#)]
6. Yang, D.; Xiao, J.; Wang, B.; Li, L.; Kong, X.; Liao, J. The immune reaction and degradation fate of scaffold in cartilage/bone tissue engineering. *Mater. Sci. Eng. C. Mater. Biol. Appl.* **2019**, *104*, 109927. [[CrossRef](#)]
7. Vishwanath, V.; Rao, H.M. Gutta-percha in endodontics—A comprehensive review of material science. *J. Conserv. Dent.* **2019**, *22*, 216–222. [[CrossRef](#)]

8. Floriano, J.F.; da Mota, L.S.; Furtado, E.L.; Rossetto, V.J.; Graeff, C.F. Biocompatibility studies of natural rubber latex from different tree clones and collection methods. *J. Mater. Sci. Mater. Med.* **2014**, *25*, 461–470. [\[CrossRef\]](#)
9. Modulevsky, D.J.; Cuerrier, C.M.; Pelling, A.E. Biocompatibility of subcutaneously implanted plant-derived cellulose biomaterials. *PLoS ONE* **2016**, *11*, e0157894. [\[CrossRef\]](#)
10. Ichhpujani, P.; Dada, T.; Bhartiya, S. Biodegradable collagen implants in trabeculectomy. *J. Curr. Glaucoma Pract.* **2015**, *9*, 24–27.
11. Voicu, G.; Ene, V.-L.; Sava, D.-F.; Surdu, V.-A.; Busuioc, C. Sol-gel derived vitroceramic materials for biomedical applications. *J. Non-Cryst. Solids* **2016**, *449*, 75–82. [\[CrossRef\]](#)
12. Jinga, S.-I.; Constantinoiu, I.; Surdu, V.-A.; Iordache, F.; Busuioc, C. Sol-gel-derived mineral scaffolds within SiO₂-P₂O₅-CaO-MgO-ZnO-CaF₂ system. *J. Sol-Gel Sci. Technol.* **2019**, *90*, 411–421. [\[CrossRef\]](#)
13. Abdelgeliel, A.S.; Ferraris, S.; Cochis, A.; Vitalini, S.; Iriti, M.; Mohammed, H.; Kumar, A.; Cazzola, M.; Salem, W.M.; Verne, E.; et al. Surface functionalization of bioactive glasses with polyphenols from *padina pavonica* algae and in situ reduction of silver ions: Physico-chemical characterization and biological response. *Coatings* **2019**, *9*, 394. [\[CrossRef\]](#)
14. Zafir, A.V.; Voicu, G.; Busuioc, C.; Jinga, S.I.; Albu, M.G.; Iordache, F. New Coll-HA/BT composite materials for hard tissue engineering. *Mater. Sci. Eng. C* **2016**, *62*, 795–805. [\[CrossRef\]](#)
15. Elias, C.N.; Lima, J.H.C.; Valiev, R.; Meyers, M.A. Biomedical applications of titanium and its alloys. *JOM* **2008**, *60*, 46–49. [\[CrossRef\]](#)
16. Liu, X.; Chen, S.; Tsoi, J.K.H.; Matinlinna, J.P. Binary titanium alloys as dental implant materials—A review. *Regen. Biomater.* **2017**, *4*, 315–323. [\[CrossRef\]](#)
17. Li, Y.; Yang, C.; Zhao, H.; Qu, S.; Li, X.; Li, Y. New developments of Ti-based alloys for biomedical applications. *Materials* **2014**, *7*, 1709–1800. [\[CrossRef\]](#)
18. Svanidze, E.; Besara, T.; Ozaydin, M.F.; Tiwary, C.S.; Wang, J.K.; Radhakrishnan, S.; Mani, S.; Xin, Y.; Han, K.; Liang, H.; et al. High hardness in the biocompatible intermetallic compound β -Ti₃Au. *Sci. Adv.* **2016**, *2*, e1600319. [\[CrossRef\]](#)
19. Mavrogenis, A.F.; Dimitriou, R.; Parvizi, J.; Babis, G.C. Biology of implant osseointegration. *J. Musculoskelet. Neuronal Interact.* **2009**, *9*, 61–71.
20. Péraire, C.; Arias, J.L.; Bernal, D.; Pou, J.; Leon, B.; Arano, A.; Roth, W. Biological stability and osteoconductivity in rabbit tibia of pulsed laser deposited hydroxylapatite coatings. *J. Biomed. Mater. Res. A* **2006**, *77A*, 370–379. [\[CrossRef\]](#)
21. Aydin, I.; Bahcepinar, A.I.; Kirman, M.; Cipiloglu, M.A. HA coating on Ti6Al7Nb alloy using an electrophoretic deposition method and surface properties examination of the resulting coatings. *Coatings* **2019**, *9*, 402. [\[CrossRef\]](#)
22. Dass, A.; Moridi, A. State of the art in directed energy deposition: From additive manufacturing to materials design. *Coatings* **2019**, *9*, 418. [\[CrossRef\]](#)
23. Voicu, G.; Miu, D.; Dogaru, I.; Jinga, S.I.; Busuioc, C. Vitroceramic interface deposited on titanium substrate by pulsed laser deposition method. *Int. J. Pharm.* **2016**, *510*, 449–456. [\[CrossRef\]](#) [\[PubMed\]](#)
24. Busuioc, C.; Voicu, G.; Zuzu, I.D.; Miu, D.; Sima, C.; Iordache, F.; Jinga, S.I. Vitroceramic coatings deposited by laser ablation on Ti-Zr substrates for implantable medical applications with improved biocompatibility. *Ceram. Int.* **2017**, *43*, 5498–5504. [\[CrossRef\]](#)
25. Negrea, R.; Busuioc, C.; Constantinoiu, I.; Miu, D.; Enache, C.; Iordache, F.; Jinga, S.-I. Akermanite based coatings grown by pulsed laser deposition for metallic implants employed in orthopaedics. *Surf. Coat. Technol.* **2019**, *357*, 1015–1026. [\[CrossRef\]](#)
26. Albargi, H.B.; Alshammari, M.S.; Museery, K.Y.; Heald, S.M.; Jiang, F.-X.; Saeedi, A.M.A.; Fox, A.M.; Gehring, G.A. Relevance of the preparation of the target for PLD on the magnetic properties of films of iron-doped indium oxide. *Coatings* **2019**, *9*, 381. [\[CrossRef\]](#)
27. Rafieerad, A.R.; Bushroa, A.R.; Nasiri-Tabrizi, B.; Baradaran, S.; Shahtalebi, S.; Khanahmadi, S.; Afshar-Mohajer, M.; Vadivelu, J.; Yusof, F.; Basirun, W.J. In-vitro bioassay of electrophoretically deposited hydroxyapatite-zirconia nanocomposite coating on Ti-6Al-7Nb implant. *Adv. Appl. Ceram.* **2017**, *116*, 293–306. [\[CrossRef\]](#)
28. Vladescu, A.; Parau, A.; Pana, I.; Cotrut, C.M.; Constantin, L.R.; Braic, V.; Vranceanu, D.M. In vitro activity assays of sputtered HAp coatings with SiC addition in various simulated biological fluids. *Coatings* **2019**, *9*, 389. [\[CrossRef\]](#)

29. Kokubo, T. Surface chemistry of bioactive glass-ceramics. *J. Non Cryst. Solids* **1990**, *120*, 138–151. [[CrossRef](#)]
30. Barbinta-Patrascu, M.E.; Badea, N.; Bacalum, M.; Ungureanu, C.; Suica-Bunghez, I.R.; Iordache, S.M.; Pirvu, C.; Zgura, I.; Maraloiu, V.A. 3D hybrid structures based on biomimetic membranes and *Caryophyllus aromaticus*—“green” synthesized nano-silver with improved bioperformances. *Mater. Sci. Eng. C* **2019**, *101*, 120–137. [[CrossRef](#)]
31. Kalinkina, E.V.; Kalinkin, A.M.; Forsling, W.; Makarov, V.N. Sorption of atmospheric carbon dioxide and structural changes of Ca and Mg silicate minerals during grinding: II Enstatite, akermanite and wollastonite. *Int. J. Miner. Process.* **2001**, *61*, 289–299. [[CrossRef](#)]
32. Zare-Harofteh, A.; Saber-Samandari, S.; Saber-Samandari, S. The effective role of akermanite on the apatite-forming ability of gelatin scaffold as a bone graft substitute. *Ceram. Int.* **2016**, *42*, 17781–17791. [[CrossRef](#)]
33. Shamoradi, F.; Emadi, R.; Ghomi, H. Fabrication of monticellite-akermanite nanocomposite powder for tissue engineering applications. *J. Alloys Comp.* **2017**, *693*, 601–605. [[CrossRef](#)]
34. Dasan, A.; Elsayed, H.; Kraxner, J.; Galusek, D.; Bernardo, E. Hierarchically porous 3D-printed akermanite scaffolds from silicones and engineered fillers. *J. Eur. Ceram. Soc.* **2019**, *39*, 4445–4449. [[CrossRef](#)]



© 2019 by the authors. Licensee MDPI, Basel, Switzerland. This article is an open access article distributed under the terms and conditions of the Creative Commons Attribution (CC BY) license (<http://creativecommons.org/licenses/by/4.0/>).